

GEOPHYSICS

Stabilization of fault slip by fluid injection in the laboratory and in situ

Frédéric Cappa^{1,2*}, Marco Maria Scuderi³, Cristiano Collettini^{3,4}, Yves Guglielmi⁵, Jean-Philippe Avouac⁶

Faults can slip seismically or aseismically depending on their hydromechanical properties, which can be measured in the laboratory. Here, we demonstrate that fault slip induced by fluid injection in a natural fault at the decametric scale is quantitatively consistent with fault slip and frictional properties measured in the laboratory. The increase in fluid pressure first induces accelerating aseismic creep and fault opening. As the fluid pressure increases further, friction becomes mainly rate strengthening, favoring aseismic slip. Our study reveals how coupling between fault slip and fluid flow promotes stable fault creep during fluid injection. Seismicity is most probably triggered indirectly by the fluid injection due to loading of nonpressurized fault patches by aseismic creep.

INTRODUCTION

Friction laws derived from laboratory experiments (1) provide a convenient framework to model fault slip whether related to natural tectonic loading (2) or induced by fluid injections (3). Hydraulic fault properties are also an important factor as variations of fluid pressure can favor seismic or aseismic slip (4–6). A number of natural faults have now been sampled from deep drill cores and characterized with laboratory measurements (7–10). It is, however, not obvious that these measurements are relevant to predict fault behavior at the larger scale. Processes might differ, and some factors not represented in the laboratory measurements (e.g., heterogeneities of mechanical and hydraulic properties and fault roughness) might determine the behavior at the larger scale.

These issues motivated us to compare laboratory and in situ observations of fault slip induced by fluid injection with the objective of testing the consistency of the results despite the scale difference and to gain insight into the influence of fluids on the model of slip. Some experiments (6, 11) and observations at geothermal sites (12, 13) and in shale gas reservoirs (14, 15) successfully documented the existence of aseismic deformations preceding seismicity during fluid injection, but the underlying physical mechanisms at the origin of aseismic creep and changes in fault properties, which might induce earthquakes during fluid injection, remain elusive.

Here, we present laboratory and in situ measurements of fault-parallel (“slip”) and fault-perpendicular (“opening”) displacement during controlled fluid injection experiments (Fig. 1). We also use laboratory experiments to characterize the fault frictional properties with increasing fluid pressure (Fig. 2) and a three-dimensional (3D) hydromechanical model to test whether these properties are consistent with the in situ observations and shed light on the origin of aseismic deformation. We formulate a fault dynamics model that couples fluid flow, permeability, and friction changes during fluid injection (Fig. 3).

¹Université Côte d’Azur, CNRS, Observatoire de la Côte d’Azur, IRD, Géoazur, 06560 Sophia Antipolis, France. ²Institut Universitaire de France, Paris, France. ³Dipartimento di Scienze della Terra, La Sapienza Università di Roma, Piazzale Aldo Moro 5, 00185 Rome, Italy. ⁴Istituto Nazionale di Geofisica e Vulcanologia, via di Vigna Murata 605, 00143 Rome, Italy. ⁵Earth and Environmental Sciences, Lawrence Berkeley National Laboratory, Berkeley, CA 94720, USA. ⁶Seismological Laboratory, California Institute of Technology, Pasadena, CA 91125, USA.

*Corresponding author. Email: cappa@géoazur.unice.fr

Copyright © 2019 The Authors, some rights reserved; exclusive licensee American Association for the Advancement of Science. No claim to original U.S. Government Works. Distributed under a Creative Commons Attribution NonCommercial License 4.0 (CC BY-NC).

RESULTS

Fault deformation during fluid injection experiments

Laboratory injection experiments were conducted with the Brittle Rock deformation Versatile Apparatus (BRAVA) (16) capable of hosting 5 cm by 5 cm fault gouge samples within a pressure vessel for true triaxial loading suitable both for fluid injection (17) and the characterization of frictional properties (18) (see Materials and Methods and figs. S1 to S4). The laboratory experiments were conducted using samples collected from the same fault that we studied in the field. The fault gouge was collected from limestone rock samples drilled

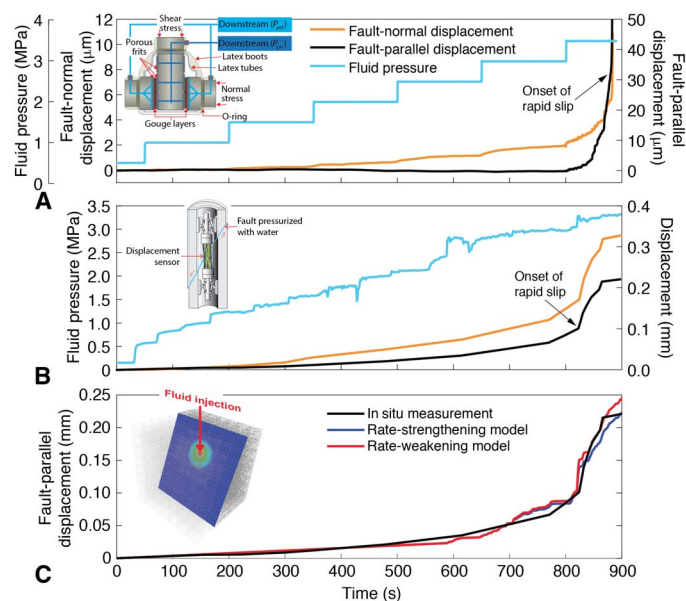


Fig. 1. Fault movements induced over time by fluid injection. Fluid pressure and fault displacements measured during fluid injection in (A) laboratory and (B) in situ experiments. (C) Agreement between observed and modeled slip and influence of the frictional model. Inset: Schematic representation of experimental devices used in this study. In the laboratory, the inset in (A) shows the double direct shear (DDS) configuration with forcing blocks equipped with hydraulic conduits for fluid injection (see Materials and Methods) (17). In the in situ experiment, the inset in (B) shows the fault displacement sensor fixed on the borehole wall in each fault compartment (see Materials and Methods) (6). In the two experiments, there is a clear dilatant fault aseismic creep that accelerates with pressurization. In the simulation, the inset in (C) shows the fault geometry and injection.

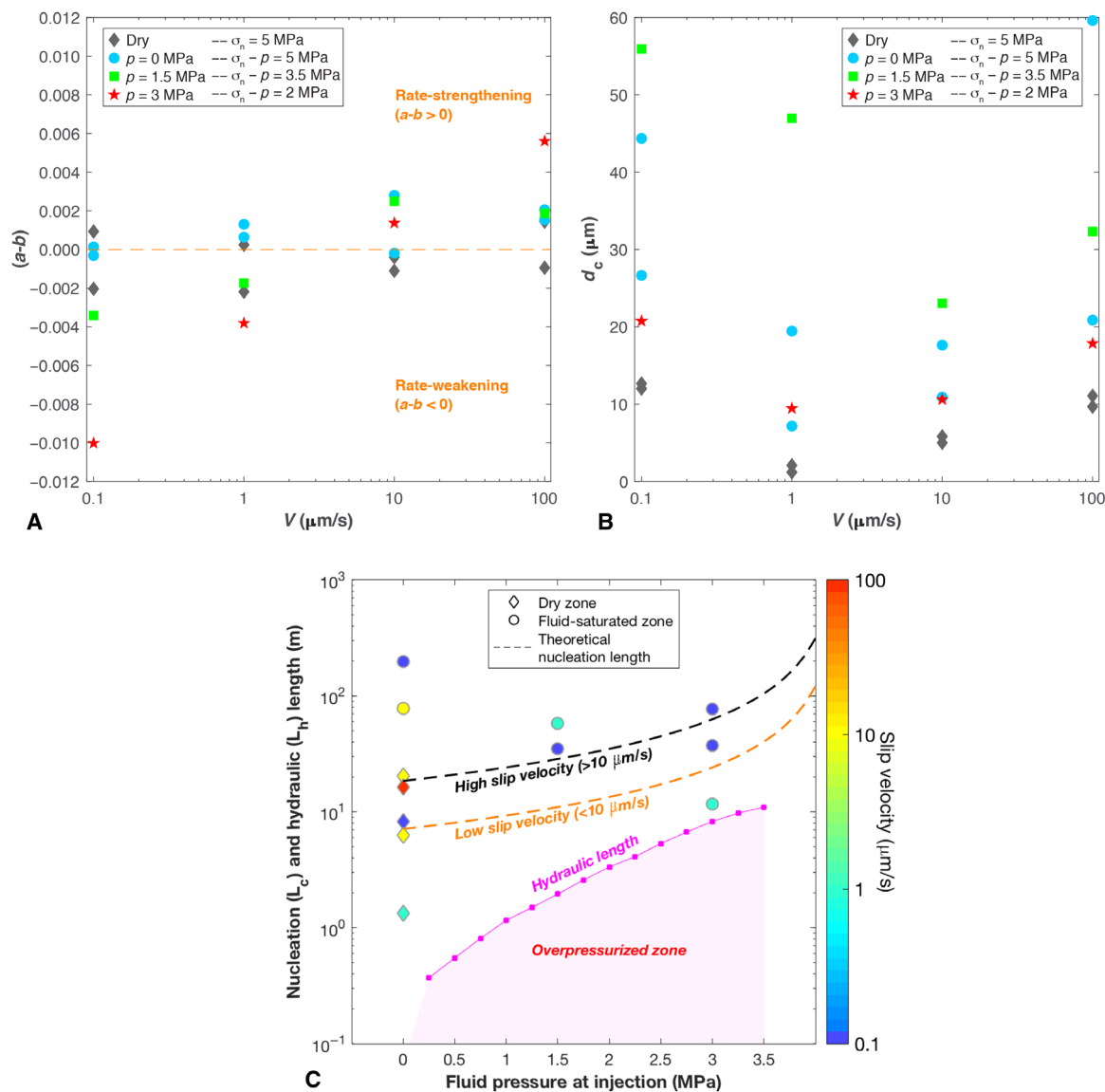


Fig. 2. Frictional properties and characteristic length for earthquake nucleation and hydraulic diffusion. (A) Rate dependence of frictional behavior as a function of slip velocity for different values of fluid pressure (p) and effective normal stress ($\sigma_n - p$). Rate weakening ($a-b < 0$) mainly occurs at low velocities ($<10 \mu\text{m/s}$), which is a necessary condition for the nucleation of seismic slip. At higher velocities, the fault mainly becomes rate strengthening ($a-b > 0$), which is indicative of a stable aseismic behavior. At fluid pressures above 1.5 MPa, the fault friction switches from rate weakening at low slip velocity (0.1 to $1 \mu\text{m/s}$) to rate strengthening at high slip velocity (10 to $100 \mu\text{m/s}$), delineating two regimes of frictional behavior. This transition means that the unstable slip is suppressed above a threshold velocity and the aseismic creep is sustained. (B) Evolution of the critical slip distance with slip velocity and fluid pressure. (C) Nucleation and hydraulic length as a function of the fluid pressure at injection. The critical nucleation length required for seismicity is calculated from Eq. 1 using the laboratory friction parameters and the in situ effective normal stress (23). The theoretical dashed lines (black and orange) are calculated using two sets of rate-and-state parameters. The parameters used are the average ($a-b$) and critical slip distance (d_c) at low slip velocity (0.1 and $1 \mu\text{m/s}$) and at high slip velocity (10 and $100 \mu\text{m/s}$). From these average values of ($a-b$) and d_c , the values of nucleation length (L_c) are then calculated over the fluid pressure range applied during the in situ experiment (0 to 3.5 MPa). The hydraulic radius is calculated from the best-fit 3D model of water injection into the fault and expresses the limits of the pressurized zone.

from a natural permeable ($k \sim 7 \times 10^{-12} \text{ m}^2$) fault with a dip angle of 70° , which we reactivated by fluid injection at a depth of 282 m in an underground gallery (see Materials and Methods and fig. S5) (6). During laboratory experiments, the fault was first loaded at a constant displacement rate to achieve steady-state frictional sliding and a well-developed shear fabric within the sample. Then, the control of the applied shear stress was changed from displacement rate to stress control to simulate the boundary conditions of a natural fault

loaded by tectonic stresses and measure the resulting fault slip. Both in the laboratory and in situ (figs. S2 and S5), faults are loaded similarly: The normal stress (σ_n) acting on the fault is ~ 4.25 MPa, the shear stress (τ) is ~ 1.2 MPa (which corresponds to about 50% of the measured shear strength), and during injection, fluid pressure (p) is progressively increased from 0 to ~ 3.5 MPa over 900 s with a similar loading path (Fig. 1, A and B). We synchronously measured the fluid pressure, fault opening, and slip. In both experiments, we observe that fault opening

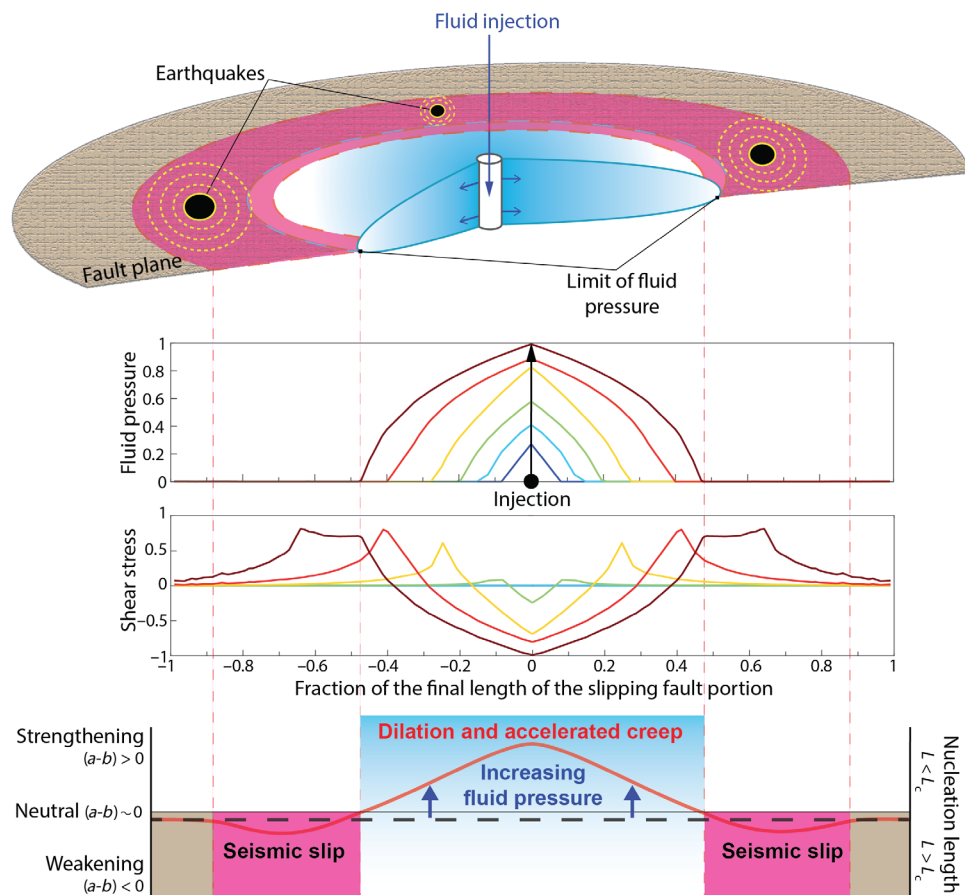


Fig. 3. Conceptual illustration of evolution of fault frictional stability during fluid injection derived from experimental evidence and numerical modeling. Initially, at low fluid pressure, the fault has a slightly rate-weakening or neutral behavior but may change to rate strengthening at and near the injection where fluid pressure and critical nucleation length (L_c) increase (red line). Fault opening and accelerating creep occur in the pressurized area, whereas at its limit and beyond, the fault remains rate weakening or neutral with a critical amount of accumulated shear stress caused by propagating creep, which, at least, helps to trigger seismic slip.

and slip evolve exponentially up to the main instability (Fig. 1, A and B). Although absolute values are different (opening of 12 and 320 μm and slip of 50 and 220 μm , for laboratory and in situ data, respectively), the general evolution of the fault volumetric deformation shows a high degree of similarity, suggesting a common underlying mechanism that is scale independent (Fig. 1, A and B). We observe a slow aseismic creep associated with fault opening ($v \leq 25 \mu\text{m/s}$ in the laboratory and up to 1 $\mu\text{m/s}$ in situ) that accelerates to $v > 25 \mu\text{m/s}$ in the laboratory and up to 5 $\mu\text{m/s}$ in situ. The slip continues to accelerate in the laboratory, whereas it decelerates in the in situ experiment. The peak in opening and creep marks the onset of rapid slip at 882 and 824 s, for laboratory and in situ data, respectively (Fig. 1, A and B).

Frictional behavior evolution with increasing fluid pressure

To further investigate the processes responsible for the observed response to the fluid injection in the laboratory and in situ, we explored how friction properties depend on the fluid pressure by conducting velocity-step tests (velocity between 0.1 and 100 $\mu\text{m/s}$) on the fault gouge. We explored the full range of fluid pressure boundary conditions from dry ($\sigma_n = 5 \text{ MPa}$) to water-saturated ($p = 0$, $\sigma_n = 5 \text{ MPa}$), pressurized fluid of $p = 1.5 \text{ MPa}$ resulting in an effective normal stress ($\sigma_n' = \sigma_n - p$) of 3.5 MPa and a subhydrostatic gradient and of $p = 3 \text{ MPa}$ resulting in an effective normal stress of 2 MPa and a suprahydrostatic gradient.

We explored these conditions since the in situ experiment started under dry conditions and then increased the fluid pressure. We determined the rate-and-state friction parameter ($a-b$) and the critical slip distance (d_c) using inversion techniques (see Materials and Methods and fig. S3) (18). Under dry and zero fluid pressure conditions, the fault has a velocity-neutral behavior on average that can slightly evolve to rate weakening or rate strengthening with slip velocity (Fig. 2A). With increasing fluid pressure ($p > 1.5$ up to 3 MPa), the fault undergoes a transition from rate-weakening to rate-strengthening friction behavior above slip velocities of $\sim 10 \mu\text{m/s}$ (Fig. 2A and table S1) and an increase of the critical slip distance from 1.2 to 59.6 μm (Fig. 2B and table S1). The large values of d_c that we measure at slow velocities (0.1 $\mu\text{m/s}$; Fig. 2B) may result from the two orders of magnitude velocity down-step (from 10 to 0.1 $\mu\text{m/s}$) and will not be considered for the following calculations. The observed evolution of frictional behavior with shear velocity is an intrinsic property of the fault gouge and is not related to shear-induced dilatancy [e.g., (4)] and the potential evolution of the fault hydrological properties as the fluid pressure is actually constant during the experiment (fig. S4). Nonetheless, since we are not measuring the fluid pressure inside the fault gouge, we cannot rule out that small variations in fluid pressure may influence the frictional behavior. These observations demonstrate that the stability of frictional sliding increases as the fault accelerates and the

effective stress decreases, highlighting that fluid pressure has a primary control on the evolution of fault frictional stability. The exact micromechanical process responsible for fluid-induced friction changes remains elusive. They could reflect granular flow with grain rotation and translation (19) enhanced during deformation at low effective stress.

Hydromechanical modeling of fault slip caused by fluid injection

To integrate laboratory and in situ measurements, we developed a 3D hydromechanical model including laboratory friction data to conduct simulations of the in situ fluid injection experiment (see Materials and Methods). We assumed a planar fault geometry with a dip of 70° in an elastic medium and used injection pressure as recorded in situ (Fig. 1B). Before injection, the fault is loaded by large-scale stresses, resulting in background shear stress (τ_0) and effective normal stress ($\sigma_{n0}' = \sigma_{n0} - p_0$). Fault slip is governed by the rate-and-state friction (μ) law (1) with a reference friction coefficient (μ_0), empirical constants (a and b), a critical slip distance (d_c), and the aging state (θ) evolution law (20). The frictional and hydraulic properties are uniform over the fault. Water injection in the fault increases the fluid pressure, which diffuses in space with time, and reduces the fault strength $\tau = \mu \cdot (\sigma_n - p)$.

The numerical solution of fault slip shows an excellent fit with the in situ measurement (Fig. 1C and fig. S6). The model implies a slip on fault that reaches a dimension of about 15 m by the time the fluid pressure is increased to 3.5 MPa. The model assumes constant a and b values. We find a good agreement between the measurements and the model predictions for either a rate-weakening or rate-strengthening behavior using parameters in the range of the values estimated experimentally. The laboratory friction data thus appear consistent with the in situ observations at the meter scale. We note, however, that the rate-weakening models ($a-b < 0$) fit better at the later part where the fluid pressure is higher and slip velocity is still less than 10 $\mu\text{m/s}$, an observation that would be consistent with the effect of fluid pressure on the frictional behavior observed in the laboratory. By reconciling fault slip and friction data, our results suggest that the mechanisms and hydromechanical properties are similar at both scales. The model (figs. S7 and S8) also shows that aseismic slip initiates within the pressurized region and then continues to develop in a sustained manner beyond the pressure front where shear strength reduces and shear stress accumulates, hence potentially triggering seismicity on earthquake-prone fault areas (Fig. 3). Our results are consistent with previous theoretical works on pressurized, rate-and-state faults, suggesting that friction weakening allows the slip to advance ahead of the pressure front (21, 22).

Nucleation theory indicates that an earthquake occurs within the rate-weakening regime once the slipping region reaches a critical size (L_c) (23)

$$L_c = \frac{Gd_c}{(\sigma_n - p)(b - a)} \quad (1)$$

where G is the rock shear modulus. For the range of injected pressures and measured friction parameters, our estimates of the critical nucleation lengths are greater than the evolution of hydraulic radius of the pressurized area despite the variations in friction parameters (Fig. 2C) (see Materials and Methods). This analysis is consistent with the slip being aseismic in the pressurized area, as observed in situ and predicted by the hydromechanical model.

DISCUSSION

Our results demonstrate that, for the slow injection rate tested here, the increase in fluid pressure can accelerate the aseismic creep. Slip remains stable, although friction may be rate weakening as the fluid pressure is increased because the pressurized zone of forced slip does not exceed the critical size for unstable slip (L_c in Eq. 1) (Fig. 2C). This aseismic behavior would occur independently of the effect of fluid pressure on the intrinsic rate-and-state parameter ($a-b$). We note, however, that any seismic slip would, in any case, die off as the friction law becomes rate strengthening at higher slip velocity and fluid pressure (Fig. 2A).

The comparison between fault slip and opening by fluid injection in the laboratory and in situ (Fig. 1) shows a different behavior after the initial phase of acceleration. This difference is attributed to the fact that, in the laboratory, fluid cannot escape in the far field, while in nature, the fluid pressure is not uniform in the extended fault zone and slip can decelerate. The smaller displacements observed in the laboratory might be due to a lesser degree of shear localization in the fault gouge. This mechanism is probably not operating in the in situ experiment made on a well-developed slip surface. In any case, both experiments demonstrate a coeval initial phase of fault opening and accelerating creep.

Existing studies of induced seismicity show that earthquakes can be triggered at a distance from injection by fluid pressure diffusion (24, 25), poroelastic stress transfer (6, 26, 27), or earthquake interactions (28, 29); the largest earthquakes can occur well after the end of injection, at a time when the effect of fluid overpressure is negligible (30). Our observations of accelerating dilatant creep provide a mechanism for earthquake triggering outside the pressurized area. Beyond injection-induced seismicity, this mechanism is consistent with the concept of aseismic creep contributing to trigger seismic rupture on faults whose friction is spatially heterogeneous (31).

We have reconciled a suite of independent measurements of fault deformation caused by fluid injection at different scales (centimeters to meters) and find that accelerating aseismic creep along permeable faults play a key role in injection-induced deformation and seismicity (Fig. 3). In addition, the observation that the friction parameters vary during fluid injection and evolve from rate weakening to rate strengthening with increasing fluid pressure provides an efficient mechanism to maintain aseismic slip in the pressurized zone. Then, earthquakes may be triggered by propagating aseismic creep that can increase shear stress to failure beyond the pressure front. Considering this interaction, physics-based models that use new friction laws including the effects of fluid pressure and its rate of change on friction parameters (32) may help to anticipate fault response to injection based on modeling and monitoring of seismicity, seismic velocity changes, and deformation (29, 33, 34).

MATERIALS AND METHODS

Laboratory fluid injection experiment

We performed laboratory experiments using a biaxial apparatus (BRAVA) configured in a double direct shear (DDS) configuration within a pressure vessel to allow a true triaxial stress field (16, 18) (fig. S1). Normal and shear stress were applied via fast-acting hydraulic servo-controlled rams. Applied loads were measured internally to the pressure vessel via strain-gauged hollowed load cells (LEANE International model CCDG-0.1-100-SPEC) positioned at the ram nose, with an accuracy of ± 0.03 kN over a maximum force of 1.5 MN, that were calibrated regularly. Displacements were measured via linear

variable displacement transformers (LVDTs), referenced at the load frame and the moving piston, with an accuracy of $\pm 0.1 \mu\text{m}$ (fig. S1A). Load point displacement measurements were corrected for the stiffness of the testing apparatus, with nominal values of 386.12 kN/mm for the vertical frame and 329.5 kN/mm for the horizontal frame. Confining pressure (P_c) and upstream and downstream fluid pressure (P_{pu} and P_{pd}) were applied using three independent hydraulic fast-acting servo-controlled intensifiers (fig. S1A). Fluid and confining pressure are measured via diaphragm pressure transducers accurate to ± 7 kPa and displacements via LVDTs. Pore fluid pressure was applied using water in equilibrium with CaCO_3 , similar to the fluid that circulates within the carbonate-bearing fault zone, and confining pressure was applied using a hydrogenated paraffinic white oil (Vaseline oil viscosity, ISO 15). All the output signals were recorded using a simultaneous multichannel analog-to-digital converter with a 24-bit channel resolution at a sampling rate of 10 kHz and then averaged for storage at rates between 1 Hz and 10 kHz. All the experiments were recorded at a minimum recording rate of 10 to 1000 Hz.

The DDS configuration consists of a three-steel block assembly that sandwiches two identical layers of powdered (grain size, $<125 \mu\text{m}$) simulated fault gouge. The forcing blocks are equipped with conduits for fluid flow that directly connect the fault gouge with the upstream and downstream fluid pressure intensifiers (fig. S1B). Sintered porous frits (permeability, $1 \times 10^{-14} \text{m}^2$) are press fit within cavities in the forcing blocks to allow a homogeneous distribution of fluids on the sample surface. The porous frits are equipped with grooves (height, 1 mm; spacing, 0.8 mm) to localize shear deformation within the gouge layers and avoid shear at the boundary. For this configuration, the nominal frictional contact area is 5.54 cm by 5.55 cm, and we refer all the measurements of stress, displacement, and pressure changes to one layer.

Samples were prepared using leveling jigs to achieve a uniform layer thickness of 5 mm. After the layers were constructed, each side of the DDS shear was weighted to ensure a uniform starting sample density (i.e., porosity). At this stage, the central block was secured to the side blocks, and the sample was jacketed to separate the gouge layers and pore fluid from the confining oil (fig. S1C) [see details in (18)]. Pore fluid pressure lines were then connected to the sample assembly and the sample positioned within the pressure vessel.

Each experiment followed a common loading up procedure. For our sample geometry and dimension, the effective normal stress (σ_n') acting on the gouge layers is given by $\sigma_n' = (\sigma_n + P_c) - P_f$. We first applied the confining pressure stepwise until we reached the target value of 4 MPa, which was maintained constant throughout the experiment. Next, we advanced the horizontal ram to apply a constant normal stress of 1 MPa that was maintained throughout the experiment by controlling the piston in a load-mode feedback control. With this configuration, we are capable to resolve fine details of the evolution of gouge layer thickness (h), after correcting for the geometrical layer thinning due to our DDS geometry [e.g., (35)]. At this point, fluid saturation begun by increasing the fluid pressure (0.5 MPa) at the upstream intensifier, while the downstream line was opened to the atmosphere. We waited for flow through, and once it was established, meaning that all the fault gouge was fully saturated, we closed the downstream intensifier to the atmosphere and waited for fluid pressure equilibration.

Injection experiments consisted of a three-stage experimental protocol (fig. S2). First, we advanced the vertical ram at a constant displacement rate of $10 \mu\text{m/s}$ until we reached a steady-state strength (fig. S2A). This stage is necessary to localize shear within the simu-

lated fault gouge. Then, we stopped the vertical ram and let the sample relax until a residual shear strength was achieved, which implies that the sample reached a best packing configuration and is representative of ancient fault zone. The third stage consists of creep deformation, where we set a constant shear stress on the fault, which, in this case, was $\sim 50\%$ relative to the steady-state strength as it was retrieved from in situ experiments, and measured the resulting fault slip. The creep test started at a constant fluid pressure value of 0.5 MPa, and we let the fault creep for 1 hour to achieve a steady secondary creep. Subsequently, the fluid pressure was increased stepwise, at steps of 0.5 MPa every 2.5 min (table S2), from the upstream intensifier, and we recorded the fluid pressure at equilibrium, after the fluid pressure front diffused within the gouge layers, at the downstream intensifiers (fig. S2C).

Laboratory friction measurements using velocity-step tests

We evaluated the stability of frictional sliding by performing velocity-step tests under a variety of boundary conditions to evaluate the effect of fluid pressure on the rate-and-state frictional parameters (fig. S3 and table S1). Experiments were performed outside the pressure vessel under room pressure-temperature-humidity ($\sim 30\%$ relative humidity) conditions and saturated conditions (i.e., zero fluid pressure). Saturated conditions were achieved by surrounding the sample with an impermeable flexible membrane and filling it with water. Under these conditions, the sample was left for ~ 1 hour under a small normal load (0.5 MPa) to ensure saturation before reaching the target value. Furthermore, we performed experiments at two different levels of fluid pressure (1.5 and 3 MPa) within the pressure vessel. The load-up procedure for these experiments was the same as described above.

Each experiment begun with a first stage where the vertical ram was advanced at a constant displacement rate of $10 \mu\text{m/s}$ until a steady-state shear strength was achieved (fig. S3). At this point, a computer-controlled velocity-step history was imposed, with a sliding velocity ranging from 0.1 to $100 \mu\text{m/s}$ and a total displacement for each velocity step of $500 \mu\text{m}$. When possible, we repeated the same sequence at different values of shear displacement (i.e., shear strain) to investigate the dependence of rate-and-state friction parameters on an accumulated strain. The velocity-step sequences were separated by a slide-hold-slide test, which we do not discuss in the present manuscript.

To investigate fault slip stability and retrieve the rate-and-state friction parameters, we modeled each velocity-step following the general formulation of the rate-and-state friction constitutive equation (1, 20, 36)

$$\mu = \mu_0 + a \ln\left(\frac{v}{v_0}\right) + b \ln\left(\frac{\theta v_0}{d_c}\right) \quad (2)$$

where μ_0 represents a reference coefficient of friction at sliding velocity v_0 ; v is the frictional slip rate; a and b are empirical constants [e.g., (37)]; d_c is the critical slip distance, which is interpreted as the distance required to renew a population of asperity contacts; and θ is the state variable, representing the average contacts lifetime. We couple Eq. 1 with a description of the state evolution that here we choose as the law proposed by (36)

$$\frac{d\theta}{dt} = -\frac{v\theta}{D_c} \ln\left(\frac{v\theta}{D_c}\right) \quad (3)$$

To take in account for the finite stiffness of our experimental apparatus and its elastic interaction with the gouge layers, we couple Eqs. 2 and 3 with the time derivative of a simple spring equation

$$\frac{d\mu}{dt} = k(v_{lp} - v) \quad (4)$$

where v_{lp} is the load point velocity and k is the stiffness (given in units of μ^{-1}) measured from the loading slope of velocity steps (38–40). Because k can slightly vary as a function of confining pressure, we determined a single value of k , usually in the range $0.005 < k < 0.008 \mu^{-1}$, for each experiment and used it for all the inversions concerning those data. To obtain rate-and-state parameters a , b , and d_c , we solved Eqs. 2 and 3 using a fifth-order Runge-Kutta numerical integration technique with an adaptive step size, with Eq. 4 as a constraint. The best-fit values of the constitutive parameters were determined using an iterative, least-squares method. For a typical model fit, the unweighted chi-square error is usually ≤ 0.0001 and the variance is $\leq 5 \times 10^{-7}$. The estimated error was calculated from the covariance matrix and expressed as 1 SD, which is usually ≤ 0.0002 . These errors are usually smaller than the uncertainties associated with experimental reproducibility.

In situ fluid injection experiment

The in situ injection experiment and its concept are detailed in (6). In short, the experiment was conducted at a depth of 282 m within the LSBB (Laboratoire Souterrain à Bas Bruit) underground laboratory in France (41). The protocol consists of injecting water at a pressure of 0 to ~3.5 MPa into a segment of an inactive ~500-m-long regional fault zone. At the location of the experiment (fig. S5), the fault has a dip angle of 70° and cuts through limestone rocks, with a strike-slip to normal cumulated slip of a few meters (42). We drilled the fault with a 20-m-long vertical borehole (diameter, 16 cm) and selected a 1.5-m-long section isolated between two inflatable packers to inject 950 liters of water in the fault. In the sealed section, we placed, on either side of the fault, a special instrument based on fiber optic Bragg sensors, the SIMFIP (Step-Rate Injection Method for Fracture In-Situ Properties) probe (43), to monitor synchronously at high frequency (500 kHz) the fluid pressure (sensitivity of 1 kPa), the flow rate (sensitivity of 0.1 liter per minute), the fault-parallel displacement (i.e., “fault slip”), and the fault-normal displacement (i.e., “fault opening”) (sensitivity of 1 μm). Three seismometers in nearby boreholes (3 to 5 m from the injection well) monitored the seismic activity. During the experiment, the temperature was 12.5°C and remained constant when water was injected. Hydraulic (i.e., porosity and permeability) and elastic properties of rock and fault were estimated from laboratory and in situ tests (6, 42). A normal stress (σ_n) of $\sim 4.25 \pm 0.5$ MPa and a shear stress (τ) of $\sim 1.65 \pm 0.5$ MPa acting on the fault were estimated (6). We used the hydraulic testing of pre-existing fractures method (44) and the nonreversible displacements measured with the SIMFIP probe to extract both the reopening pressure and the slip vector on the reactivated fault planes and inverse the stresses from these measurements using a forward fully coupled numerical analysis of 10 tests (6, 11).

Nucleation length

The theoretical nucleation length (L_c) using the rate-and-state friction law (23) is defined by Eq. 1, where G is the rock shear modulus defined by $E/[2(1 + \nu)]$: E is the Young’s modulus of the rock surrounding the fault surface ($E = 20$ GPa), ν is the Poisson’s ratio ($\nu = 0.33$), d_c is the

critical slip distance ($d_c = 10 \mu\text{m}$) over which the state parameter evolves, σ_n is the normal stress ($\sigma_n = 4.25$ MPa), p is the fluid pressure ($p = 0$ to 3.5 MPa), and a and b are the rate-and-state parameters for steady-state velocity [$a-b = -0.0026$ on average at low slip velocity ($v < 10 \mu\text{m/s}$) and $a-b = -0.001$ on average at high slip velocity ($v > 10 \mu\text{m/s}$)]. Slipping patches with radii greater than the critical nucleation length $L > L_c$ are susceptible to trigger seismicity, whereas those with radii $L < L_c$ are not.

From the analysis of seismic events recorded during 11 injection tests performed in different sections of the same fault zone at similar pressures tested in the present study (11), we inferred an estimated source radius ranging from 0.19 to 0.57 m and moment magnitudes between -4.2 and -3.14 . Seismic events were located between 1 and 12 m from injections, with some clusters that are independent of fluid pressure diffusion and, rather, related to stress perturbation. In this series of experiments, the accuracy of the earthquake locations is estimated to be 1.5 m (11). Here, the size of the nucleation zone below the low slip velocity limit (~ 1.325 to 8 m) is generally consistent with theoretical estimates, but the source radius of the seismic events (0.19 to 0.57 m) observed in (11) is an order of magnitude smaller than the theoretical minimum length over which earthquake nucleation can occur. Our assumption is that the stability of fault and the transition between seismic and aseismic slip are likely controlled, at least, by local rapid stressing rate and friction weakening over short distances on small earthquake-prone fault areas that may radiate seismic waves. This is consistent with previous laboratory experiments on meter-sized rocks that investigated interactions between aseismic slip, stress changes, and seismicity on a critically stressed fault during the nucleation of stick-slip instability (45).

Modeling assumptions and parameters

We used the 3DEC code (46), a distinct element method (47), to simulate the interaction between fluid flow and fault slip evolution, including hydromechanical coupling and rate- and state-dependent friction. The model incorporates the full coupling between fluid pressure diffusion and effective stress- and strain-dependent permeability. The method has been previously used to understand the hydromechanical behavior of fractured rocks during fluid injection (48) and to study earthquake rupture and off-fault fracture response (49).

Our 3D model considers a fluid injection into a fault (dip angle of 70°) in a homogeneous elastic and impervious medium (Fig. 1C). The fault geometry reproduces the conditions of the in situ experiment (6). The remote normal (σ_n) and shear stress (τ) resolved on the fault plane are constant. During injection, the fluid pressure is increased into the fault in a point source using the loading path applied during the in situ experiment (blue curve in Fig. 1B). The initial value of stress ($\sigma_{no} = 4.25$ MPa, $\tau_o = 1.65$ MPa) and fluid pressure ($p_o = 0$) into the fault represents the conditions of the in situ experiment (6). At time $t = 0$, water is injected into the fault so that the effective normal stress within the fault is defined by $\sigma_n' = \sigma_n - p$.

This model is based on the cubic law to describe the coupling between the fluid pressure and fault normal displacement (50)

$$Q(t) = \frac{(b_{ho} + u_n)^3 \cdot w \cdot \Delta p}{12\mu_f \cdot L} \quad (5)$$

where $Q(t)$ is the flow rate (in m^3/s), w denotes the fault width (in m), b_{ho} is the initial hydraulic aperture of the fault (in m), u_n is the fault normal displacement (in m), μ_f is the fluid dynamic viscosity (in Pa·s),

L is the contact length of the fault surface (in m), and Δp is the fluid pressure change (in Pa). The fluid pressure perturbation follows a diffusivity equation

$$\Delta \dot{p} = \frac{T}{S} \nabla^2 p \quad (6)$$

where T is the transmissivity

$$T = \frac{(b_h + u_n)^3}{12\mu_f} \quad (7)$$

and S is the storativity

$$S = \left(\frac{b_h}{K_f} + \frac{1}{K + 4/3G} \right) \quad (8)$$

where b_h is the hydraulic aperture ($b_{ho} + u_n$) (in m), K_f is the fluid bulk modulus (in Pa), and K and G are the rock bulk and shear moduli (in Pa), respectively.

The magnitude of the pressure perturbation and the hydraulic properties affect the dynamics of the transient. We use an initial hydraulic aperture ($b_{ho} = 9 \times 10^{-6}$ m) consistent with an initial fault permeability of 7×10^{-12} m² estimated in situ (4), $K_f = 2$ GPa, $K = 20$ GPa, $G = 7.5$ GPa, $g = 9.81$ m/s², $\rho_f = 1000$ kg/m³, and $\mu_f = 1 \times 10^{-3}$ Pa·s.

For the frictional behavior of the fault, the model is based on the rate-and-state friction law (Eq. 2) derived from laboratory experiments (1, 20, 36). The state evolution law is described by the aging law (20)

$$\frac{d\theta}{dt} = 1 - \frac{v\theta}{d_c} \quad (9)$$

Consistent with our laboratory measurements at low slip velocity ($v < 10$ μm/s), here, we assume a rate-weakening fault with $\mu_o = 0.6$, $a = 0.001$, $b = 0.003$, and $d_c = 10$ μm. The frictional resistance of the fault is then given by

$$\tau = \mu(v, \theta)(\sigma_n - p) \quad (10)$$

SUPPLEMENTARY MATERIALS

Supplementary material for this article is available at <http://advances.sciencemag.org/cgi/content/full/5/3/eaau4065/DC1>

Fig. S1. Experimental configuration for fluid injection and fault slip in the laboratory.

Fig. S2. Experimental procedure during laboratory injection.

Fig. S3. Representative records (coefficient of friction versus shear displacement) of a velocity-stepping friction experiment.

Fig. S4. Frictional response to velocity steps and relationship with fault dilation during a typical fluid pressurized experiment.

Fig. S5. Experimental conditions of the in situ injection into the natural fault at a depth of 282 m within the LSBB underground laboratory.

Fig. S6. Sensitivity of the best-fit numerical solution to measurements obtained with a rate-weakening fault model (see Fig. 1C) while varying the parameter and the critical slip distance.

Fig. S7. Model results.

Fig. S8. Model results.

Table S1. Summary of experiments and boundary conditions used during two series of velocity steps to evaluate frictional parameters (μ_{ss} , μ_o , a , b , and d_c).

Table S2. Summary of boundary conditions during the creep experiment.

Reference (51)

REFERENCES AND NOTES

1. C. Marone, Laboratory-derived friction laws and their application to seismic faulting. *Annu. Rev. Earth Planet. Sci.* **26**, 643–696 (1998).
2. N. Lapusta, S. Barbot, Models of earthquakes and aseismic slip based on laboratory-derived rate and state friction laws, in *The Mechanics of Faulting: From Laboratory to Real Earthquakes*, A. Bizzarri, H. S. Bhat, Eds. (Research Signpost, 2012), pp. 153–207.
3. J. H. Dieterich, K. B. Richards-Dinger, K. A. Kroll, Modeling injection-induced seismicity with the physics-based earthquake simulator RSQSim. *Seismol. Res. Lett.* **86**, 1102–1109 (2015).
4. P. Segall, J. R. Rice, Dilatancy, compaction, and slip instability of a fluid-infiltrated fault. *J. Geophys. Res.* **100**, 22155–22171 (1995).
5. H. Noda, N. Lapusta, Three-dimensional earthquake sequence simulations with evolving temperature and pore pressure due to shear heating: Effect of heterogeneous hydraulic diffusivity. *J. Geophys. Res.* **115**, B12314 (2010).
6. Y. Guglielmi, F. Cappa, J. P. Avouac, P. Henry, D. Elsworth, Seismicity triggered by fluid injection-induced aseismic slip. *Science* **348**, 1224–1226 (2015).
7. W. Tanikawa, T. Shimamoto, Frictional and transport properties of the Chelungpu fault from shallow borehole data and their correlation with seismic behavior during the 1999 Chi-Chi earthquake. *J. Geophys. Res.* **114**, N01502 (2009).
8. B. M. Carpenter, C. Marone, D. M. Saffer, Weakness of the San Andreas fault revealed by samples from the active fault zone. *Nat. Geosci.* **4**, 251–254 (2011).
9. M. J. Ikari, J. Kameda, D. M. Saffer, A. J. Kopf, Strength characteristics of Japan Trench boreholes samples in the high-slip region of the 2011 Tohoku-Oki earthquake. *Earth Planet. Sci. Lett.* **412**, 35–41 (2015).
10. A. R. Niemeijer, C. Boulton, V. G. Toy, J. Townend, R. Sutherland, Large-displacement, hydrothermal frictional properties of DFD-1 fault rocks, Alpine Fault, New Zealand: Implications for deep rupture propagation. *J. Geophys. Res.* **121**, 624–647 (2016).
11. L. Duboeuf, L. De Barros, F. Cappa, Y. Guglielmi, A. Deschamps, S. Seguy, Aseismic motions drive a sparse seismicity during fluid injections into a fractured zone in a carbonate reservoir. *J. Geophys. Res.* **122**, 1–10 (2017).
12. F. H. Cornet, J. Helm, H. Poitrenaud, A. Etchecopar, Seismic and aseismic slips induced by large-scale fluid injections. *Pure Appl. Geophys.* **150**, 563–583 (1997).
13. S. Wei, J.-P. Avouac, K. W. Hudnut, A. Donnellan, J. W. Parker, R. W. Graves, D. Helmberger, E. Fielding, Z. Liu, F. Cappa, M. Eneva, The 2012 Brawley swarm triggered by injection-induced aseismic slip. *Earth Planet. Sci. Lett.* **422**, 115–125 (2015).
14. M. D. Zoback, A. Kohli, I. Das, M. W. McClure, The importance of slow slip on faults during hydraulic fracturing stimulation of shale gas reservoirs, in *SPE Americas Unconventional Resources Conference*, Pittsburgh, Pennsylvania, 5 to 7, June, 2012.
15. A. Kumar, E. Zorn, R. Hammack, W. Harbert, Long-period, long-duration seismicity observed during hydraulic fracturing of the Marcellus Shale in Greene County, Pennsylvania. *The Leading Edge* **36**, 580–587 (2017).
16. C. Colletini, G. Di Stefano, B. Carpenter, P. Scarlato, T. Tesei, S. Mollo, F. Trippetta, C. Marone, G. Romeo, L. Chiaraluce, A novel and versatile apparatus for brittle rock deformation. *Int. J. Rock Mech. Min. Sci.* **66**, 114–123 (2014).
17. M. M. Scuderi, C. Colletini, C. Marone, Frictional stability and earthquake triggering during fluid pressure stimulation of an experimental fault. *Earth Planet. Sci. Lett.* **477**, 84–96 (2017).
18. M. M. Scuderi, C. Colletini, The role of fluid pressure in induced vs. triggered seismicity: Insights from rock deformation experiments on carbonates. *Sci. Rep.* **6**, 24852 (2016).
19. B. M. Carpenter, C. Colletini, C. Viti, A. Cavallo, The influence of normal stress and sliding velocity on the frictional behaviour of calcite at room temperature: Insights from laboratory experiments and microstructural observations. *Geophys. J. Int.* **205**, 548–561 (2016).
20. J. H. Dieterich, Modeling of rock friction: 1. Experimental results and constitutive equations. *J. Geophys. Res.* **84**, 2161–2168 (1979).
21. M. W. McClure, R. N. Horne, Investigation of injection-induced seismicity using a coupled fluid flow and rate/state friction model. *Geophysics* **76**, 181–WC181–WC198 (2011).
22. V. S. Gischig, Rupture propagation behavior and the largest possible earthquake induced by fluid injection into deep reservoirs. *Geophys. Res. Lett.* **42**, 7420–7428 (2015).
23. C. H. Scholz, *The Mechanics of Earthquakes and Faulting* (Cambridge Univ. Press, ed. 2, 2002).
24. W. L. Ellsworth, Injection-induced earthquakes. *Science* **341**, 1225942 (2013).
25. K. M. Keranen, M. Weingarten, G. A. Abers, B. A. Bekins, S. Ge, Sharp increase in central Oklahoma seismicity since 2008 induced by massive wastewater injection. *Science* **345**, 448–451 (2014).
26. P. Segall, S. Lu, Injection-induced seismicity: Poroelastic and earthquake nucleation effects. *J. Geophys. Res.* **120**, 5082–5103 (2015).
27. T. H. W. Goebel, M. Weingarten, X. Chen, J. Haffener, E. E. Brodsky, The 2016 Mw5.1 Fairview, Oklahoma earthquakes: Evidence for long-range poroelastic triggering at >40 km from fluid disposal wells. *Earth Planet. Sci. Lett.* **472**, 50–61 (2017).

28. F. Catali, A. P. Rinaldi, V. Gischig, M. Nespole, S. Wiemer, The importance of earthquake interactions for injection-induced seismicity: Retrospective modeling of the Basel Enhanced Geothermal System. *Geophys. Res. Lett.* **43**, 4992–4999 (2016).
29. M. Schoenball, W. L. Ellsworth, A systematic assessment of the spatiotemporal evolution of fault activation through induced seismicity in Oklahoma and Southern Kansas. *J. Geophys. Res.* **122**, 10189–10206 (2017).
30. J. H. Healy, W. W. Rubey, D. T. Griggs, C. B. Raleigh, The Denver earthquakes. *Science* **161**, 1301–1310 (1968).
31. J. P. Avouac, From geodetic imaging of seismic and aseismic fault slip to dynamic modeling of the seismic cycle. *Annu. Rev. Earth Planet. Sci.* **43**, 233–271 (2015).
32. J. Chen, A. R. Niemeijer, Seismogenic potential of a gouge-filled fault and the criterion for its slip stability: Constraints from a microphysical model. *J. Geophys. Res.* **122**, 9658–9688 (2017).
33. D. Rivet, L. De Barros, Y. Guglielmi, F. Cappa, R. Castilla, P. Henry, Seismic velocity changes associated with aseismic deformations of a fault stimulated by fluid injection. *Geophys. Res. Lett.* **43**, 9563–9572 (2016).
34. M. Shirzaei, W. L. Ellsworth, K. F. Tiampo, P. J. Gonzalez, M. Manga, Surface uplift and time-dependent seismic hazard due to fluid injection in eastern Texas. *Science* **353**, 1416–1419 (2016).
35. D. R. Scott, C. J. Marone, C. G. Sammis, The apparent friction of granular fault gouge in sheared layers. *J. Geophys. Res.* **99**, 7231–7246 (1994).
36. A. L. Ruina, Slip instability and state variable friction laws. *J. Geophys. Res.* **88**, 10359–10370 (1983).
37. M. J. Ikari, B.M. Carpenter, C. Marone, A microphysical interpretation of rate- and state- dependent friction for fault gouge. *Geochem. Geophys. Geosyst.* **17**, 1660–1677 (2016).
38. L. Reinen, J. D. Weeks, Determination of rock friction constitutive parameters using an iterative least squares inversion method. *J. Geophys. Res.* **98**, 15937–15950 (1993).
39. M. L. Blanpied, C. J. Marone, D. A. Lockner, J. D. Byerlee, D. P. King, Quantitative measure of the variation in fault rheology due to fluid-rock interaction. *J. Geophys. Res.* **103**, 9691–9712 (1998).
40. D. M. Saffer, C. Marone, Comparison of smectite- and illite-rich gouge frictional properties: Application to the updip limit of the seismogenic zone along subduction megathrusts. *Earth Planet. Sci. Lett.* **215**, 219–235 (2003).
41. Laboratoire Souterrain à Bas Bruit; www.lsbbeu.fr.
42. P. Jeanne, Y. Guglielmi, J. Lamarche, F. Cappa, L. Marie, Architectural characteristics and petrophysical properties evolution of a strike-slip fault zone in a fractured porous carbonate reservoir. *J. Struct. Geol.* **44**, 93–109 (2012).
43. Y. Guglielmi, F. Cappa, H. Lançon, J. B. Janowczyk, J. Rutqvist, C. F. Tsang, J. S. Y. Wang, ISRM suggested method for step-rate injection method for fracture in-situ properties (SIMFIP): Using a 3-components borehole deformation sensor. *Rock Mech. Rock Eng.* **47**, 303–311 (2014).
44. B. C. Haimson, F.H. Cornet, ISRM suggested methods for rock stress estimation; Part 3: Hydraulic fracturing (HF) and/or hydraulic testing of pre-existing fractures (HTPF). *Int. J. Rock Mech. Min. Sci.* **40**, 1011–1020 (2003).
45. G. C. McLaskey, B. D. Kilgore, Foreshocks during the nucleation of stick-slip instability. *J. Geophys. Res.* **118**, 2982–2997 (2013).
46. Itasca Consulting Group Inc. *3DEC 3-Dimensional Distinct Element Code* (ICG, 2016).
47. P. A. Cundall, Formulation of a three-dimensional distinct element model—Part I. A scheme to detect and represent contacts in a system composed of many polyhedral blocks. *Int. J. Rock Mech. Min. Sci. Geomech. Abstr.* **25**, 107–116 (1988).
48. F. Cappa, Y. Guglielmi, J. Rutqvist, C.-F. Tsang, A. Thoraval, Hydromechanical modelling of pulse tests that measure fluid pressure and fracture normal displacement at the Coaraze Laboratory site, France. *Int. J. Rock Mech. Min. Sci.* **46**, 1062–1082 (2006).
49. B. Fäth, H. Hökmark, B. Lund, P. M. Mai, R. Roberts, R. Munier, Simulating earthquake rupture and off-fault fracture response: Application to the safety assessment of the Swedish nuclear waste repository. *Bull. Seismo. Soc. Am.* **105**, 134–151 (2015).
50. P. A. Witherspoon, J. S. Y. Wang, K. Iwai, J. E. Gale, Validity of cubic law for fluid flow in a deformable rock fracture. *Water Resour. Res.* **16**, 1016–1024 (1980).
51. J. Samuelson, D. Elsworth, C. Marone, Shear-induced dilatancy of fluid-saturated faults: Experiment and theory. *J. Geophys. Res.* **114**, B12404 (2009).

Acknowledgments: We thank M. Violay and J. Hazzard for fruitful discussions and P. Segall and one anonymous reviewer for constructive comments. **Funding:** The research presented in this paper is supported by the Agence Nationale de la Recherche (ANR) through the “HYDROSEIS” project under contract no. ANR-13-JS06-0004-01. F.C. was partially supported by the Institut Universitaire de France, and by the French government, through the UCAJEDI Investments in the Future project managed by the ANR with reference no. ANR-15-IDEX-01 at the Université Côte d’Azur. Laboratory experiments have been funded by ERC grant no. 259256 GLASS to C.C. and Marie Skłodowska-Curie grant no. 656676 FEAT to M.M.S. **Author contributions:** All authors contributed to the data analysis, discussions and interpretations of results, and writing of the article. F.C. conceived the original idea, led the study, conducted the in situ experiment, and developed the hydromechanical modeling. M.M.S. and C.C. conducted the laboratory experiments and data processing. Y.G. conducted the in situ experiment and data processing. J.-P.A. contributed to the model development and analysis of data and modeling results. **Competing interests:** The authors declare that they have no competing interests. **Data and materials availability:** All data needed to evaluate the conclusions in the paper are present in the paper and/or the Supplementary Materials. Additional data related to this paper may be requested from the authors. Data are also housed in the Géoazur laboratory, Université Côte d’Azur, France (email: cappa@geoazur.unice.fr).

Submitted 7 June 2018
Accepted 30 January 2019
Published 13 March 2019
10.1126/sciadv.aau4065

Citation: F. Cappa, M. M. Scuderi, C. Colletini, Y. Guglielmi, J.-P. Avouac, Stabilization of fault slip by fluid injection in the laboratory and in situ. *Sci. Adv.* **5**, eaau4065 (2019).

Stabilization of fault slip by fluid injection in the laboratory and in situ

Frédéric Cappa, Marco Maria Scuderi, Cristiano Colletini, Yves Guglielmi and Jean-Philippe Avouac

Sci Adv 5 (3), eaau4065.

DOI: 10.1126/sciadv.aau4065

ARTICLE TOOLS

<http://advances.sciencemag.org/content/5/3/eaau4065>

SUPPLEMENTARY MATERIALS

<http://advances.sciencemag.org/content/suppl/2019/03/11/5.3.eaau4065.DC1>

REFERENCES

This article cites 46 articles, 6 of which you can access for free
<http://advances.sciencemag.org/content/5/3/eaau4065#BIBL>

PERMISSIONS

<http://www.sciencemag.org/help/reprints-and-permissions>

Use of this article is subject to the [Terms of Service](#)

Science Advances (ISSN 2375-2548) is published by the American Association for the Advancement of Science, 1200 New York Avenue NW, Washington, DC 20005. 2017 © The Authors, some rights reserved; exclusive licensee American Association for the Advancement of Science. No claim to original U.S. Government Works. The title *Science Advances* is a registered trademark of AAAS.